JACS
JOURNAL OF THE AMERICAN CHEMICAL SOCIETY
Article
pubs.acs.org/JACS

Investigating Sodium Storage Mechanisms in Tin Anodes: A Combined Pair Distribution Function Analysis, Density Functional Theory, and Solid-State NMR Approach

Joshua M. Stratford,[†] Martin Mayo,[‡] Phoebe K. Allan,[†,§,∥] Oliver Pecher,[†] Olaf J. Borkiewicz,[⊥] Kamila M. Wiaderek,[⊥] Karena W. Chapman,[⊥] Chris J. Pickard,[#,▽] Andrew J. Morris,*[,‡,□] and Clare P. Grey*[,†]

[†]Department of Chemistry, University of Cambridge, Lensfield Road, Cambridge CB2 1EW, U.K.
[‡]Cavendish Laboratory, University of Cambridge, J. J. Thomson Avenue, Cambridge CB3 0HE, U.K.
[§]Gonville and Caius College, Trinity Street, Cambridge CB2 1TA, U.K.
[∥]Diamond Light Source Ltd., Harwell Science and Innovation Campus, Didcot OX11 0DE, U.K.
[⊥]X-ray Science Division, Advanced Photon Source, Argonne National Laboratory, Argonne, Illinois 60439, United States
[#]Department of Materials Science and Metallurgy, University of Cambridge, 27 Charles Babbage Road, Cambridge CB3 0FS, U.K.
[▽]Advanced Institute for Materials Research, Tohoku University, 2-1-1 Katahira, Aoba-ku, Sendai 980-8577, Japan
[□]Department of Physics, University of Warwick, Gibbet Hill Road, Coventry CV4 7AL, U.K.

Supporting Information

ABSTRACT: The alloying mechanism of high-capacity tin anodes for sodium-ion batteries is investigated using a combined theoretical and experimental approach. *Ab initio* random structure searching (AIRSS) and high-throughput screening using a species-swap method provide insights into a range of possible sodium−tin structures. These structures are linked to experiments using both average and local structure probes in the form of *operando* pair distribution function analysis, X-ray diffraction, and ^{23}Na solid-state nuclear magnetic resonance (ssNMR), along with *ex situ* ^{119}Sn ssNMR. Through this approach, we propose structures for the previously unidentified crystalline and amorphous intermediates. The first electrochemical process of sodium insertion into tin results in the conversion of crystalline tin into a layered structure consisting of mixed Na/Sn occupancy sites intercalated between planar hexagonal layers of Sn atoms (approximate stoichiometry $NaSn_3$). Following this, $NaSn_2$, which is predicted to be thermodynamically stable by AIRSS, forms; this contains hexagonal layers closely related to $NaSn_3$, but has no tin atoms between the layers. $NaSn_2$ is broken down into an amorphous phase of approximate composition $Na_{1.2}Sn$. Reverse Monte Carlo refinements of an *ab initio* molecular dynamics model of this phase show that the predominant tin connectivity is chains. Further reaction with sodium results in the formation of structures containing Sn−Sn dumbbells, which interconvert through a solid-solution mechanism. These structures are based upon $Na_{5-x}Sn_2$, with increasing occupancy of one of its sodium sites commensurate with the amount of sodium added. ssNMR results indicate that the final product, $Na_{15}Sn_4$, can store additional sodium atoms as an off-stoichiometry compound ($Na_{15+x}Sn_4$) in a manner similar to $Li_{15}Si_4$.

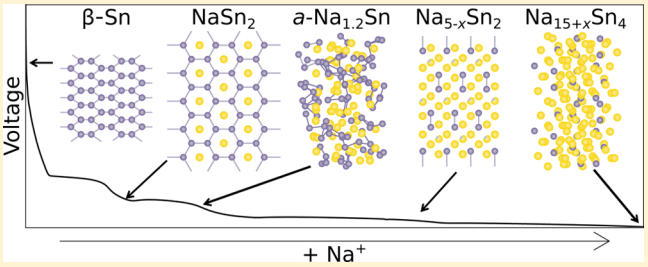

INTRODUCTION

Sodium-ion batteries are an attractive option for many electrochemical devices owing to the low cost and high abundance of sodium. Furthermore, the lack of an alloying reaction with aluminum at low potentials prevents the need for expensive copper current collectors.[1,2] Graphite is used as an anode material in the majority of existing lithium-ion batteries. However, it shows very little capacity for sodium.[3] Alloying materials, such as Sn, Sb, Ge, and Pb, are of great interest because of their large gravimetric capacities: practical reversible capacities of 500, 580, 350, and 480 mAh g^{-1}, respectively, have previously been reported over multiple cycles, with theoretical capacities even greater.[4−6] Tin shows a very high theoretical capacity of 847 mAh g^{-1} (based on complete conversion to $Na_{15}Sn_4$), and reported experimental capacities have been able to approach this.[4,7] Furthermore, it has frequently been employed in binary systems, such as SnSb, CoSn, and SnS, which can offer improved long-term performance.[8−12] Efforts to understand these more complex systems will be aided by a

Received: February 9, 2017
Published: May 4, 2017

DOI: 10.1021/jacs.7b01398
J. Am. Chem. Soc. 2017, 139, 7273−7286

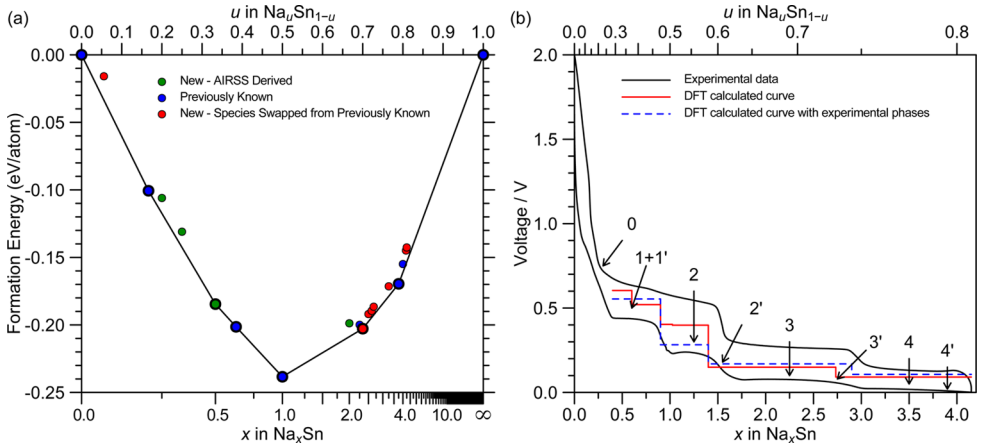

Figure 1. (a) Formation enthalpy per atom vs sodium concentration in the Na−Sn compound. The convex hull (tie-line) is constructed by joining the stable structures obtained by the searches. Only the lowest energy structure for each composition within 0.02 eV/atom from the convex hull are shown. (b) Electrochemistry data for a sodium−tin cell cycled at a rate of $C/20$ (corresponding to achieving a capacity of 847 mAh g^{-1} in 20 h) between 2 and 0.001 V (black line). Observed electrochemical processes are indicated with arrows. Average potentials relative to sodium metal calculated for the structures found on the convex hull are shown as red lines calculated by DFT. The blue line corresponds to the potentials calculated by DFT using structures which best fit the experimental observations (namely $NaSn_2$, *a*-NaSn, Na_5Sn_2, and $Na_{15}Sn_4$). The theoretical profiles are aligned with the experimental profile (removing process "0") such that it starts with process 1. Experimental data are normalized (to allow ready comparison with theory) such that 3.75 Na are inserted (and removed) during processes 1 through 4′ (data plotted vs capacity may be found in Figure S1). As the linear *x*-axes for (a) and (b) differ according to the requirements of the functions plotted, secondary axes are included to allow ready comparison between them.

detailed understanding of the nature of sodium storage in the single-component tin system.

The electrochemical properties of the sodium−tin system were first investigated in 1920 when four NaSn alloys were discovered through electrochemical reactions in pyridine solutions, namely Na_4Sn, Na_2Sn, NaSn, and $NaSn_2$ (i.e., $Na_{0.5}Sn$).[13] Molten sodium batteries with tin counter-electrodes were investigated in the early 1990s, identifying three single-phase alloy regions and determining their approximate compositions.[14] A patent application in 2007 used tin as the anode in a full-cell configuration.[15] Recent intense interest in the sodium−tin electrochemical system began in 2011 when a theoretical voltage profile of Na−Sn was calculated by Chevrier et al. using known crystal structures from the Inorganic Crystal Structure Database (ICSD),[16] including $NaSn_5$, NaSn, Na_9Sn_4, and $Na_{15}Sn_4$ (i.e., $Na_{0.2}Sn$, NaSn, $Na_{2.25}Sn$, and $Na_{3.75}Sn$, respectively).[3] A subsequent experimental work presented a galvanostatic electrochemical profile with four distinguishable plateaus, which were assigned to the mechanism proposed by Chevrier et al., although there was a large discrepancy between the calculated and experimental results.[4] Ellis et al. proposed a slightly different mechanism for the first plateau, where a composition of $NaSn_3$ was determined by coulometry.[17] The authors were the first to identify the formation of an amorphous species of approximate composition NaSn and also demonstrate the formation of additional crystalline intermediates, but, with the exception of $Na_{15}Sn_4$, their diffraction patterns do not match those of any known structures for these phases. An *operando* transmission electron microscopy (TEM) study of tin nanoparticles suggested a different phase transformation: a first step two-phase reaction from pristine Sn to amorphous $NaSn_2$, followed by single-phase reactions resulting in amorphous Na_9Sn_4 and Na_3Sn phases, and finally a crystalline $Na_{15}Sn_4$ phase.[18] It should be noted that significant differences in the experimental setup used in the TEM study, such as a solid NaOH + Na_2O electrolyte in place of a conventional liquid electrolyte and the use of potential rather than current control, could have an effect on the observed sodium insertion mechanism.[19] Work by Baggetto et al. on tin thin films showed a more complex form of the electrochemical potential profile.[7] The first process around 0.4 V was shown to be composed of two processes on discharge, but only a single process on charge. Their experimental work was accompanied by a density functional theory (DFT) calculation of theoretical voltages using the known Na−Sn phases and metastable phases generated using the cluster-expansion method. Using X-ray diffraction (XRD), they furthered previous analysis by assigning the DFT calculated Na_5Sn_2−$R\bar{3}m$ (where $R\bar{3}m$ refers to the space group, specified here to distinguish between different possible polymorphs) structure to the phase formed at the end of the third process. In a more recent study, the same group performed a reinvestigation of Na_xSn phases with $x \geq 1$.[20] The XRD pattern of a phase synthesized by solid-state reaction methods matched Na_7Sn_3−$R\bar{3}m$, a defect variant of the Li_5Sn_2−$R\bar{3}m$ structure with sodium substituted for lithium; therefore it was postulated that this, not Na_5Sn_2, is the product of the electrochemical reaction with tin. The authors proposed that Na_7Sn_3 formed at the expense of the thermodynamically stable Na_9Sn_4−*Cmcm* phase due to its slow formation kinetics.

Clearly, there remain significant gaps in understanding of the phases formed during sodium insertion. In the following, we present an investigation into these phases using a combination of structure prediction, combining *ab initio* random structure searching (AIRSS)[21,22] with high-throughput screening from the ICSD, and experiment. The unique capability of AIRSS to access metastable phases enables us to explore the Na−Sn system and predict new structures. *Operando* measurements circumvent problems associated with sample degradation, which can complicate the interpretation of *ex situ* data, and can additionally observe metastable intermediates that may be subject to relaxation effects during post-mortem analysis. We use *operando* XRD, pair distribution function (PDF) analysis, and solid-state NMR (ssNMR) to probe both local structure and longer-range in order to analyze the structure of the phases

DOI: 10.1021/jacs.7b01398
J. Am. Chem. Soc. 2017, 139, 7273−7286

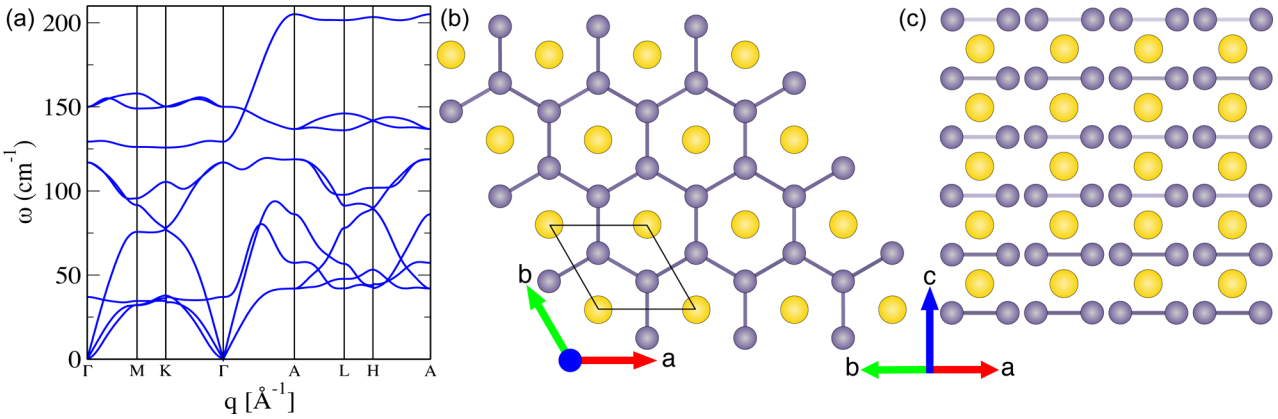

Figure 2. (a) Phonon dispersion curve of $NaSn_2$—*P6/mmm*. The absence of any imaginary frequency in the Brillouin zone confirms the stability of a structure in terms of lattice dynamics. (b) A projection of the $NaSn_2$ structure viewed down the *c*-axis. (c) A projection of the $NaSn_2$ structure viewed down the (110) plane; sodium atoms are shown in yellow, tin in gray.

formed. In particular, the following questions are addressed: (i) the number and nature of the crystalline phase(s) formed during the first electrochemical process, about which little is known; (ii) the structural features of the amorphous phase formed during the second electrochemical process; and (iii) the phase formed during the third process, where there remains a lack of consensus within the literature—Na_9Sn_4, Na_7Sn_3, and Na_3Sn, have all been suggested as potential candidates.

RESULTS

Theory Overview. In Figure 1a, we present a plot of formation enthalpy as a function of sodium concentration for the structures obtained by AIRSS and the swapping species method. For clarity, only the lowest energy structures, within 0.02 eV/atom of the tie-lines are included. The tie-lines are defined by connecting the points depicting the lowest energy structures found, such that the overall tie-line function is convex (i.e., forming a convex hull). A description of these structures is found in Table S1. Despite the existence of a low-temperature (thermodynamic) phase of tin, α-Sn, we have used the metastable phase β-Sn to set the chemical potential since the latter is used experimentally as the battery anode. The convex hull construction predicts the following stable phases: $NaSn_5$ ($P\bar{4}2_1m$), $NaSn_2$ (*P6/mmm*), Na_5Sn_8 (*P2/c*), NaSn ($I4_1/acd$), Na_7Sn_3 ($P32_12$), and $Na_{15}Sn_4$ ($I\bar{4}3d$). Of these, the structures of $NaSn_5$, Na_5Sn_8, NaSn, and $Na_{15}Sn_4$ have been experimentally reported.[23−26] In addition, a number of metastable phases are identified, with energies close to the convex hull. In Figure 1b, we present the voltage curve calculated from these stable structures, which exhibits a reasonable agreement with an experimentally obtained curve.

The convex hull shows three stable structures with a sodium content $\leq Na_{0.5}Sn$: $NaSn_5$,[23] Na_5Sn_8[24] ($Na_{1.17}Sn_2$ with partial occupancies set to one), and a $NaSn_2$—*P6/mmm* structure obtained by AIRSS. The predicted $NaSn_2$—*P6/mmm* structure (AlB_2 structure type) has a formation energy 0.015 eV/atom lower than the experimentally known $NaSn_2$—*C2/m* Zintl phase.[27] Baggetto et al. obtained a series of phases with the $NaSn_2$ composition, using a cluster-expansion method.[7] They provided a total of 27 different structures in the Supporting Information, of which four are reported to have stoichiometry $NaSn_2$. One of these phases (*P2/m*) actually has a stoichiometry of Na_1Sn_1, the remaining three having space groups *C2/c*, $P2_1/m$, and $P6_3/mmc$. They are all similar in terms of Sn−Sn connectivity to our *P6/mmm* structure, but differ in containing irregular hexagons or nonplanar layers. The closest match is their monoclinic $P2_1/m$ phase, which was not included within their analysis of the Na−Sn convex hull. Relaxation of this structure with the DFT level of theory presented here led to another local minima with *Cmmm* symmetry, rather than our *P6/mmm* structure. Given the large number of structurally related phases with this composition, we have assessed the dynamical stability of our *P6/mmm* structure by performing a phonon calculation using density-functional perturbation theory in CASTEP (full details can be found in the Experimental Methods).[28] The obtained dispersion shown in Figure 2a shows no negative frequencies suggesting that the phase is dynamically stable at 0 K. The convergence of the phonon dispersion with respect to the BZ point sampling was found to be very slow, particularly the mode corresponding to the out-of-plane Sn vibrations. Using a spacing of 0.03 $Å^{-1}$ led to imaginary frequencies in the vicinity of q = 0,0,0.5 $Å^{-1}$. A spacing of 0.0175 $Å^{-1}$ was found to be sufficient to converge the phonon dispersion, probably hinting at a strong coupling between phonon modes and the Fermi surface. $NaSn_2$ was also identified in a recent DFT study, where it was predicted to be at least metastable under ambient conditions.[29] In this region we further identify three metastable structures within 0.02 eV/atom of the convex hull: $NaSn_{17}$ which was obtained by swapping species from $Na_{0.40}Si_{17}$[30] with partial occupancies set to 1, and two AIRSS structures: $NaSn_4$—*Cc* and $NaSn_3$—$Pm\bar{3}m$. Phases with a stoichiometry of $NaSn_4$ and $NaSn_3$ have been observed as shown in the Na−Sn phase diagram,[31] nevertheless no crystal structure of these phases has been reported experimentally. Our predicted $NaSn_4$ and $NaSn_3$ structures exhibit similar connectivity to that found in $NaSn_5$, being mainly composed of a 3-D network of Sn atoms. We note that this AIRSS- derived $NaSn_3$ structure is distinct from the phase of the same stoichiometry discussed later as part of the experimental results. The experimentally known Na_5Sn_{13} structure also falls within this composition range,[32] but is found 0.023 eV/atom from the convex hull, which is above our 0.02 eV/atom cutoff, and is therefore not included in our analysis.

Moving to higher concentrations, Na_1Sn_1—$I4_1/acd$ is the only stable phase found in Na_xSn $0.5 < x < 2$. Beyond this (Na_2Sn to $Na_{3.5}Sn$), the structures exhibit Sn−Sn dumbbells. Our DFT calculations predict that the Na_7Sn_3 phase, obtained by

DOI: 10.1021/jacs.7b01398
J. Am. Chem. Soc. 2017, 139, 7273−7286

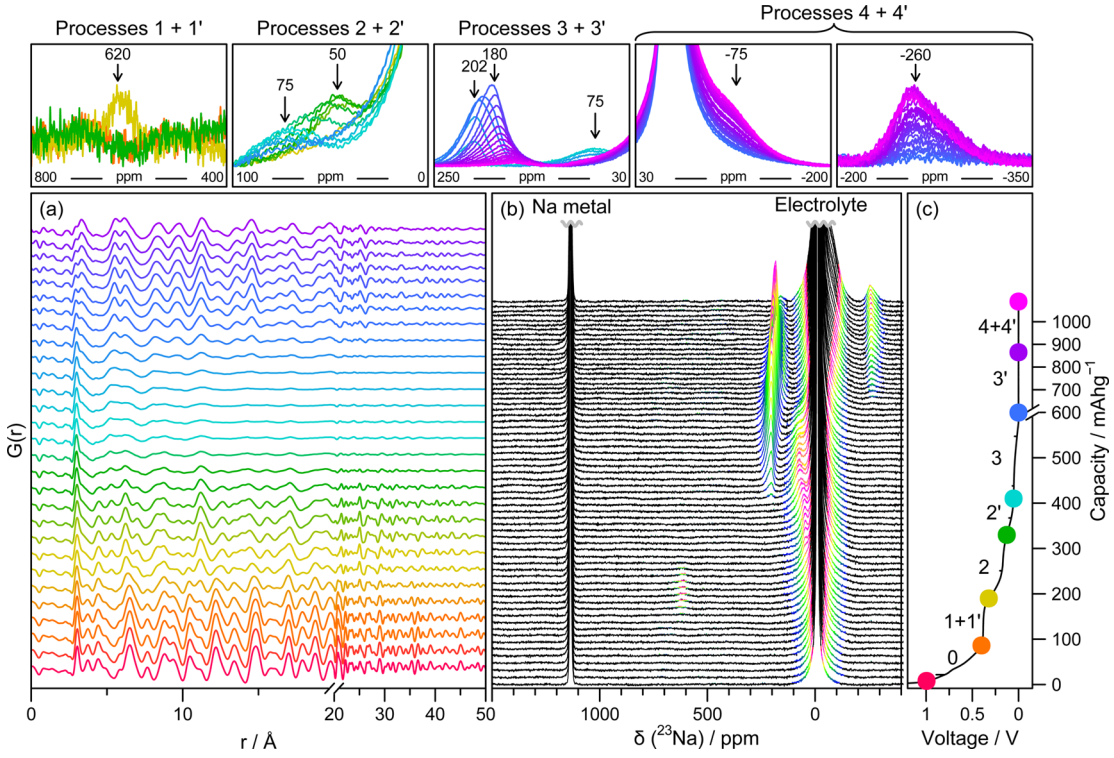

Figure 3. *Operando* measurements for electrochemical cells with sodium metal and tin electrodes, and a $NaPF_6$ electrolyte. (a) Selected PDFs obtained during the first discharge are vertically offset in time; the colors correspond to the points shown on the electrochemical curve. (b) ^{23}Na NMR spectra obtained during the first discharge, aligned with the corresponding electrochemistry (c). Strong features corresponding largely to the electrolyte or metal have been truncated for clarity. Spectra are colored in the region −500 to 1000 ppm according to their intensity. Selected regions are highlighted above, where the colors now correspond to the points shown on the electrochemical curve. The cells were cycled at a rate of *C*/30 (corresponding to achieving a capacity of 847 mAh g^{-1} in 30 h) between 2 and 0.001 V, and held at the end of discharge until the current dropped to below *C*/100.

swapping species from Li_7Si_3−$P3_212$, is stable whereas the experimentally reported Na_9Sn_4[33] phase is found 4 meV/atom above the convex hull tie-line.

The lowest sodium content structure in this region is a metastable Na_2Sn−$P2_1/c$ AIRSS structure. The structure is formed of non-collinear Sn−Sn dumbbells. The Na_7Sn_3 and Na_9Sn_4 structures mentioned above are found on increasing in sodium further, followed by Na_5Sn_2, $Na_{13}Sn_5$, Na_8Sn_3, and $Na_{13}Sn_4$. All these metastable structures are very close to the tie-line of the convex hull construction. The concentration of Sn−Sn dumbbells in Na_2Sn, Na_9Sn_4, Na_7Sn_3, and Na_5Sn_2 is gradually lowered as Na concentration is increased, forming a mixture of Sn−Sn dumbbells and isolated atoms in $Na_{13}Sn_5$, Na_8Sn_3, and $Na_{13}Sn_4$. This tendency to form a series of structurally related dumbbell-containing compounds has been observed in the Li−Si[34] and Li−Ge[34,35] systems, and we refer the reader to reference 34 for a detailed description of the structures. Of course, a difference is observed in the dumbbell distances compared to the Li−Si,Ge systems, however, a similar trend is observed, as is shown in Figure S15: the distance of the Sn−Sn dumbbells increases with Na concentration reaching a maximum at Na_5Sn_2, at this concentration the dumbbells start to break up allowing the remaining Sn−Sn dumbbells to relax.

At the highest sodium concentrations (>$Na_{3.5}Sn$) we find the stable $Na_{15}Sn_4$−$I\bar{4}3d$ phase, along with three metastable phases at higher sodium concentrations: Na_4Sn−*Pnma* (which is a known Na−Sn phase with partial occupancies set to one), $Na_{21}Sn_5$−$F\bar{4}3m$, and $Na_{17}Sn_4$−$F\bar{4}3m$ which were obtained by swapping species from LiSn phases. All these structures contain isolated Sn atoms.

In the following sections, we interpret our experimental data in the context of the phases shown on this hull.

Electrochemical Results. Figure 1b shows the experimental galvanostatic electrochemical profile obtained at a rate of *C*/20 and a temperature of 55 °C. In agreement with previous reports, we observe multiple electrochemical processes; we denote these as processes 0, 1, 2, 3, and 4, and these names will be used throughout the subsequent text. We also note that there are sloping regions toward the end of processes 2, 3, and 4, which account for a significant fraction of the capacity at these potentials. We refer to these as 2′, 3′, and 4′, respectively. The reasons underlying these distinctions will be discussed in the following sections. In addition, Baggetto et al. note the possibility that the first electrochemical process on discharge (around 450 mV) may in fact be two distinct processes;[7] we refer to these as processes 1 followed by 1′.

Overview of *Operando* Results. *Operando* PDF data, obtained by the Fourier transformation of X-ray total scattering data, are shown in Figure 3a. It is apparent that the pristine material (*β*-Sn) initially undergoes very little change (electrochemical process 0), which is followed by a transformation of *β*-Sn into one or more crystalline phases, with correlations extending beyond 50 Å (electrochemical processes 1 and 1′). The loss of extended connectivity during electrochemical processes 2 and 2′ is clear, with no major correlations found beyond 20 Å in this region. Finally, a return to long-range ordering is observed throughout the remaining electrochemical

DOI: 10.1021/jacs.7b01398
J. Am. Chem. Soc. 2017, 139, 7273−7286

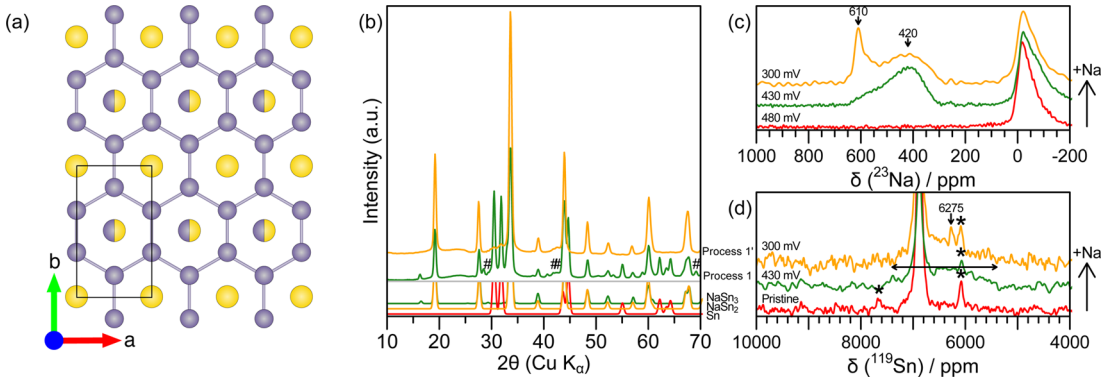

Figure 4. (a) A projection of the $NaSn_3$—*Pmmm* structure viewed down the *c*-axis, demonstrating the structural similarity to $NaSn_2$. Sodium atoms are shown in yellow, tin atoms in gray, and mixed occupancies are shown as a mixture of yellow and gray. (b) Frames from an *operando* XRD experiment taken at the end of electrochemical processes 1 (green) and 1′ (orange). Note in particular the peak at 16.5° in the data for process 1, which, along with others, cannot derive from $NaSn_2$. Calculated patterns are shown below for Sn (red), $NaSn_2$ (orange), and $NaSn_3$ (green) (large peaks have been truncated for clarity), trace amounts of Na from the cell background are indicated by #. Data were gathered using X-rays of wavelength 0.1430 Å and converted to Cu Kα (1.54 Å). *Ex situ* (c) ^{23}Na and (d) ^{119}Sn 60 kHz MAS NMR spectra of tin anodes discharged to 480 mV (bottom, red), 430 mV (middle, green), and 300 mV (top, orange). Intensities have been normalized based on the sample mass and number of transients collected. Spinning sidebands are indicated with an asterisk (*). In (c) shifts are indicated for peaks not resulting from SEI, sodium inserted into the Super P carbon additive or sodium within the CMC binder (these constitute the broad peak between approximately −100 to 0 ppm). In (d) the shift of the peak arising from $NaSn_2$ is indicated at 6275 ppm. The broad peak arising from the $NaSn_3$ intermediate is indicated by a horizontal arrow. The strong peak resulting from β-Sn at 6890 ppm has been truncated for clarity.

processes. In addition, it is clear that the sharp Sn—Sn nearest-neighbor peak, at approximately 3 Å, is not observed to change significantly during processes 0 through 3′.

Figure 3b shows the *operando* ^{23}Na NMR spectra obtained during the first discharge. Peaks at −10 and 1140 ppm are observed throughout the measurement, including in the spectrum of the as-assembled electrochemical cell, and correspond to the $NaPF_6$ electrolyte and the sodium metal counter electrode, respectively. During electrochemical processes 1 and 1′, we observe the growth of a weak peak with a maximum at 620 ppm. This signal disappears, and a new resonance is observed at 50 ppm during process 2. Throughout process 2′, the peak at 50 ppm broadens and shifts to 75 ppm; it then shrinks as a further sodium environment is formed with a peak at a shift of 202 ppm, which corresponds to the phase formed during the third electrochemical process. The sloping region of the electrochemistry that follows, i.e. process 3′, sees this resonance shift gradually to 180 ppm. The final processes during discharge (processes 4 and 4′) result in the appearance of two additional sodium environments. We see a very broad resonance with maximum around −75 ppm, and a further peak with maximum around −260 ppm which appears later. The majority of the resonances observed have a shift whose magnitude is greater than 100 ppm; this is ascribed to the Knight shift, which is caused by the interaction of unpaired electrons at the Fermi level of the conduction band interacting with the nuclear spins.[36] The shift is a measure of the density of states at the Fermi level at the Na nucleus, and is indicative of metallic character of the material.

We now discuss the *operando* PDF and NMR results, in conjunction with additional *operando* XRD data together for each distinct electrochemical process, from 0 through to 4′.

Process 0. A slope from 1.4 V to around 0.5 V is observed in the electrochemistry. No significant capacity has been reported as a result of sodium—tin alloying reactions at these potentials. We, thus, attribute this capacity to three factors that do not involve Sn (hence our naming of this process as process 0): electrolyte decomposition to form a solid electrolyte interphase (SEI) layer, and sodium storage within the carbon additive are both commonly observed at these potentials.[37,38] In addition, *operando* XRD data for the pristine material indicates small amounts of SnO and SnO_2 are present in addition to β-Sn (Figure S2). During this period of the electrochemistry, our diffraction data indicates that SnO and SnO_2 convert sequentially into Sn metal (SI). Na_2O is also expected to form, but the low concentration compared with the bulk β-Sn, along with the much smaller X-ray structure factors of Na and O compared with Sn meant that we were unable to detect this. These reactions have previously been observed to result in a sloping electrochemical curve starting at 1 and 0.8 V, respectively, and ending around 0.5 V in both cases.[39,40] As these reactions result in the formation of β-Sn, the material that we are investigating, the presence of these side-reactions prior to the reaction of tin metal is highly unlikely to impact our subsequent results.

^{23}Na *operando* ssNMR measurements during this process show no significant changes. This is consistent with forming very small amounts of Na_2O (δ = 55.1 ppm[41]), which would give a signal too weak to show above the noise. Refinements of PDF data during this process indicate an increasingly good match to β-Sn (Table S2), consistent with the loss of the impurity oxide phases. Refinements were not made with either of the oxides as secondary phases owing to the very small concentrations observed in the Bragg diffraction data.

Processes 1 and 1′. The next feature in the electrochemistry is observed at approximately 450 mV vs Na metal and appears as a flat plateau. During this step, intensity of the peaks associated with initial Sn in the XRD/PDF patterns progressively decrease, and peaks from a new phase start to appear (Figure 3). PDF and diffraction data for the phase remaining at the end of this process provide an excellent match to the layered (*P6/mmm*) $NaSn_2$ structure (Figures 4b, S4, and S8). This structure consists of honeycomb-like layers of tin separated by layers of sodium, whose atoms sit at the center of the tin hexagons (Figure 2b,c). To the best of our knowledge, this structure has not previously been experimentally observed.

DOI: 10.1021/jacs.7b01398
J. Am. Chem. Soc. 2017, 139, 7273−7286

It should be noted that, while a diffraction pattern for the pure $NaSn_2$ phase has not been previously reported, patterns showing reflections consistent with this phase, along with one or more additional phases, have. A model has yet to be presented that explains these data.[7,17]

^{23}Na *operando* NMR measurements reveal a single peak with a shift of approximately 620 ppm, whose shift does not vary during this electrochemical process. The highly Knight shifted peak indicates a non-zero density of states at the Sn nuclei, consistent with metallic properties of this material and the extended tin structure. This is similar to the observed Knight shift for graphite intercalation compounds, whose structures show a good deal of similarity to $NaSn_2$.[42]

There is some debate in the literature as to whether a second, overlapping, plateau may also be present at a similar potential.[7] This is based upon electrochemical measurements of very thin films and is not resolvable in our electrochemical data. In order to investigate more closely whether it is possible to isolate two distinct phases forming in this region, we performed a second *operando* measurement. To increase the number of data points acquired, a cell was cycled considerably more slowly (a rate of *C*/70 was used), and data suitable for PDF analysis and higher resolution diffraction data were gathered alternately (either PDF or XRD once every hour). Bragg reflections corresponding to Sn decrease in intensity in this region as sodium is inserted, while reflections corresponding to a further two phases grow. It is unclear whether the two phases appear sequentially or concurrently, however, at the end of this region of the electrochemistry, only one—$NaSn_2$—remains (Figure S3). Our diffraction data are, therefore, in agreement with the observation of two conjugated plateaus.

The PDF data obtained during these processes (which we now distinguish as process 1 followed by 1′) can be modeled simply as a combination of Sn (whose Bragg reflections are clearly observed in our diffraction data until the end of these two processes) and $NaSn_2$ at all points (SI). This suggests that any additional intermediate must be structurally related to either Sn or $NaSn_2$, or is only present in very small concentrations. However, these two phases alone are not sufficient to reproduce the Bragg reflections observed (Figure 4b). In particular, the reflections at 16.4, 28.5, 38.0, and 40.8°, along with further peaks at higher angles, cannot derive from the $NaSn_2$–*P6*/*mmm* structure.

The additional reflections are consistent with a structure similar to $NaSn_2$, retaining the honeycomb-like tin layers, but with a reduction in symmetry resulting from the loss of the 6-fold rotation axis. As this phase is formed prior to $NaSn_2$, it must have a lower sodium content. We, therefore, generated lower symmetry structures solely through careful placement of the sodium atoms between the tin layers. However, all such structures we tried were unable to produce any significant intensity for the additional reflections. Intensity for these reflections can only be generated through changes to the tin structure.

It is clear from the PDF that there is no significant deviation from the honeycomb-like tin layers, we therefore tested a model in which tin partially occupies sites within the sodium layers. It is possible to account for the lowered symmetry by replacing every other sodium atom in the $NaSn_2$ structure with a mixed $Na_{0.5}Sn_{0.5}$ occupancy in a *Pmmm* configuration (Figure 4a). This results in a stoichiometry of $NaSn_3$, which is consistent with that expected from the electrochemistry, and with a previous study using coulometry.[17] Although this structure does contain the additional reflections in the diffraction pattern, there remain minor differences in intensity (Figure 4b). This may be an artifact of the experimental setup (e.g., preferred orientation effects). In order to assess the stability of this structure, we generated a Na_4Sn_8 supercell of $NaSn_2$–*P6*/*mmm* in which we exchanged one sodium atom for a tin atom to give a stoichiometry of $NaSn_3$ (Na_3Sn_9). This phase was relaxed using the same DFT level of theory as used in the convex hull construction. The resulting $NaSn_3$–*Pmmm* structure was converged without any major ionic rearrangement and is found at only 0.007 eV/atom from the convex hull tie-line.

While the *operando* ^{23}Na ssNMR measurement (Figure 3) revealed a single peak, higher resolution measurements using *ex situ* ^{23}Na magic angle spinning (MAS) ssNMR (Figure 4c) contained an additional asymmetrical broad feature with a maximum around 420 ppm. This signal could not be observed in the static *operando* measurement, the additional line broadening caused by the lack of MAS presumably leading to a broad feature that disappears into the baseline. An additional sharp peak at 610 ppm emerges following further sodium insertion. *Ex situ* ^{119}Sn MAS ssNMR spectra (Figure 4d) show a sharp peak at 6890 ppm corresponding to residual Sn metal and a broad resonance centered around 6600 ppm. With higher sodium content, a sharp peak at 6275 ppm emerges. The sharp resonance in spectra of both nuclei is assigned to the $NaSn_2$ structure; the broad features reduce in intensity toward the end of the processes and are consistent with disordered sodium and tin atoms between the more ordered honeycomb-like tin layers in the phases with stoichiometry close to $NaSn_3$.

Therefore, we tentatively assign the first electrochemical process (1) to the formation of a phase similar to $NaSn_2$ of approximate composition $NaSn_3$, consisting of tin layers separated by disordered layers of mixed sodium and tin occupancy. Following this, $NaSn_2$–*P6*/*mmm* forms during process 1′. Owing to the similarity of the structures formed, it is possible that process 1′ begins before process 1 has gone to completion as a result of an overpotential within the electrochemical cells.

Processes 2 and 2′. PDF measurements reveal that the process(es) at approximately 220 mV result in the breakdown of almost all long-range structure, forming an amorphous solid. The stoichiometry of this phase has previously been suggested to be approximately $Na_{1.2}Sn$.[7,17] As PDF is a total scattering technique, which does not rely on long-range order, our measurements are able to probe some structural features of the amorphous intermediate. A PDF measurement taken at the end of these processes (Figure 5) reveals relatively strong features at low *r*, which rapidly decay with increasing *r*. Beyond approximately 15 Å, peaks in the PDF are approximately constant, with the decay in intensity consistent with instrument resolution as opposed to limited particle size. This would be consistent with having two phases present: a short-range, more disordered phase with a correlation length around 15–30 Å, and a more ordered phase with a much greater correlation length. Similar behavior has been observed in the sodium–antimony and lithium–FeOF systems.[43,44] Alternatively, it is possible that such a PDF could be generated through very anisotropic disorder. In this situation, the decay in intensity at low *r* would be caused by strong disorder in one or two lattice directions, with a greater degree of ordering in the remaining direction(s) resulting in the retention of peaks at higher *r*.

DOI: 10.1021/jacs.7b01398
J. Am. Chem. Soc. 2017, 139, 7273–7286

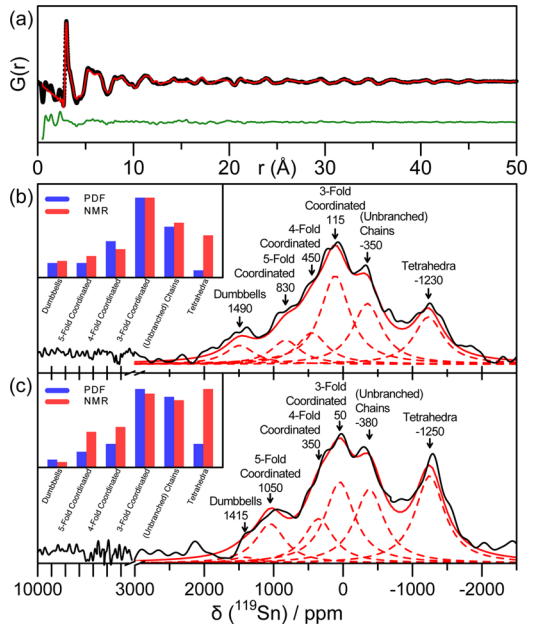

Figure 5. (a) PDF of a single frame from our *operando* experiment showing the intermediate formed at the end of processes 2 and 2′ on discharge. Two phases can be observed in the PDF: a short-range, disordered phase below approximately 15 Å, and a longer-range phase whose peaks are clearly visible beyond 15 Å. Experimental data are shown as black circles, the red line represents the calculated PDF, with its difference to the experimental PDF offset below in green. (b,c) *Ex situ* ^{119}Sn 60 kHz MAS ssNMR spectra of tin discharged to the end of processes 2 (200 mV) and 2′ (120 mV), respectively. Experimental data are shown as solid black lines, deconvolutions are shown as red dashed lines, with arrows indicating the shifts and assignment of the deconvolved peaks. The overall fit is indicated with a solid red line. Data are plotted in the ranges −2500 to 3000 ppm and 3000−10000 ppm. Inset: Histograms detailing the relative areas of the deconvolved peaks (red) along with the relative concentrations of each Sn−Sn connectivity in the structures refined against PDF measurements (blue). The PDF and NMR derived concentrations of each connectivity match well, with the exception of tetrahedral connectivity. We ascribe this discrepancy to the relaxation of this metastable intermediate into the thermodynamically stable NaSn phase, which is based on tin tetrahedra, relaxation occurring during the elapsed time between the end of the cell discharge, disassembly of the cell, and the *ex situ* NMR measurement.

The strongest peak in the PDF, present at 3.00 Å, can only be the result of tin−tin connectivity. Such a peak would be present in extended structures such as $NaSn_2$, as well as one-dimensional chains of tin atoms, tin tetrahedra or tin dumbbells. Na_1Sn_1−$I4_1/acd$ is the only stable phase found with a sodium concentration between $Na_{0.5}Sn$ and Na_2Sn. NaSn consists of tin tetrahedra; however, the inter-tetrahedra distances present in this structure are inconsistent with peaks found at higher *r* (Figure S9). This is also reflected in the difference between the DFT voltage curve (based upon the thermodynamically stable crystalline NaSn phase) and the experimental curve as seen in Figure 1b.

In order to investigate the nature of this amorphous structure, we generated an Na_1Sn_1 amorphous phase using *ab initio* molecular dynamics as described in the Experimental Methods section. Using this structure as a starting point, we performed a reverse Monte Carlo (RMC) refinement of a 10×10×10 supercell against a single scan from our *operando* PDF experiment, taking into account both real- and reciprocal-space data. Using only minimum distance constraints (based upon the measured PDF data) we were able to successfully reproduce the disordered (short-range) phase in the observed PDF.

RMC cannot readily be used to produce a complete model for materials, such as this, with both amorphous and crystalline components. We therefore performed additional real-space refinements using a least-squares method combining both a 61 atom subcell of the RMC refined $Na_{1.18}Sn$ model along with the crystalline phase described later. We used this method to quantify how the structure changed during the electrochemical process. Full details may be found in the SI.

As RMC refinements are typically highly dependent upon the initial conditions, and the resulting model does not necessarily represent a unique solution, it is important to assess the quality of this model through complementary experiments. In order to do so, we performed ^{119}Sn MAS ssNMR measurements on samples discharged to the end of these processes. The chemical shift is highly dependent on the Sn−Sn connectivity. We compared the relative concentration of each Sn−Sn connectivity in structures refined against PDF measurements during processes 2 and 2′ (blue histograms in Figure 5b,c) with the peak areas of the corresponding deconvolved NMR spectra (red histograms in Figure 5b,c). Spectra were fit using six Lorentzian curves, each with identical half widths at half maxima. The shifts for tin atoms in dumbbell or tetrahedral environments were derived from measurements on model compounds (SI) with the remaining deconvolved peaks being tentative assignments based on the agreement with the expected concentrations and the ordering of the peaks.

Results are shown in Figure 5. As it is not possible to quantify all sources of error in the measurements and fitting, the discrepancies between the results from the two different techniques represent a measure of this error. There is reasonable agreement between the expected form of the spectrum and the measured data for every connectivity excluding tetrahedra. In both NMR spectra, we observe a much stronger signal from tetrahedra than would be expected from the amount present in the model structures. A small amount of relaxation of the *ex situ* sample to the thermodynamically stable NaSn structure is likely, which accounts, at least in part, for the larger amount of tetrahedrally coordinated tin observed in the NMR spectra than the PDF derived models.

Ex situ ^{23}Na measurements (SI) reveal a similar trend, with significant intensity in two major regions in addition to the signal resulting from SEI, sodium incorporated into carbon, and CMC located around −17 ppm. These two regions are at approximately 19 ppm, which we assign to sodium atoms near four-coordinate tin (tetrahedra) and 70 ppm, which corresponds to sodium near tin chains.

^{23}Na *operando* NMR measurements (Figure 3) corresponding to process 2 reveal a resonance at a shift of 45 ppm which grows throughout the process. During process 2′, the peak is observed to continually shift and broaden until it reaches 70 ppm. Combined, these observations suggest that a more ordered structure is formed at the start of the process, which then undergoes a solid-solution type phase transition into a more disordered structure consistent with observations of an amorphous structure formed in this region.

The periodic longer-range correlations found in the PDF data result from a more ordered component of this phase. They are consistent with the correlations found within structures

DOI: 10.1021/jacs.7b01398
J. Am. Chem. Soc. 2017, 139, 7273−7286

based upon $NaSn_2$, but with significant changes required relative to the phase formed at the end of the first processes. A reduction in the *a*-lattice parameter is required, along with an expansion of the *c*-lattice parameter and a significant increase in the anisotropic thermal displacement parameter for tin in the *c*-lattice direction. While it was not possible to refine sodium occupancies or positions owing to their very small contribution to the PDF, the expansion of the interlayer distances (*c*-direction) could be a result of additional sodium atoms between the tin layers. The increased thermal displacement parameter is indicative of changes to the planarity of the layers, likely resulting in significant changes to the electrical properties of the material. It is worth noting that similar effects in other systems are used as a means of electrochemical exfoliation.[45]

Performing further refinements based upon the intermediate PDF scans reveals that the changes in lattice parameters of the $NaSn_2$ structure occur when the electrochemical profile changes from a flat plateau-like region to a more sloping region (i.e., during process 2′). Sloping regions in electrochemical profiles indicate solid-solution mechanisms, this is consistent with the observed changes to the $NaSn_2$ structure. The shifting and broadening peak observed in the *operando* ^{23}Na ssNMR measurement further shows that the local environment around the sodium atoms is changing (i.e., a solid-solution mechanism) and becoming more disordered. The relatively low values of the NMR shift compared with other NaSn phases indicates that this material is much less metallic.

We tentatively suggest that processes 2 results in the formation of an amorphous structure consisting primarily of chains of tin atoms, with the higher-order connectivities observed as a result of branching within the chains. Further insertion of sodium atoms during process 2′ occurs between the tin layers of any remaining $NaSn_2$, causing an expansion of the interlayer distances and disordering in the *c*-lattice direction.

We have further studied the effect of this amorphous NaSn structure on the voltage curve as presented in Figure 1b, where the blue voltage curve is calculated using the structures which best fit our experimental observations. The predicted voltage for a crystalline NaSn phase is significantly higher than the experimental value. Using our amorphous model instead provides a better match to the observed electrochemical profile.

Processes 3 and 3′. During these electrochemical processes, the return to long-range ordering is evident from our PDF data. The low *r* data are consistent with Sn−Sn dumbbells (Figure S14) as expected based upon the stable phases we predict in this regime of sodium concentration (Figure 1a). The simulated PDFs for all known structures containing parallel dumbbells are very similar below approximately 10 Å. However, differences in the sodium content of the phases causes differences in longer-range ordering.

Our *operando* ^{23}Na ssNMR experiment indicates that these processes do not result in the formation of a single structure with fixed stoichiometry. We first see a single peak grow with a fixed shift of 203 ppm throughout process 3. However, upon reaching the end of the plateau, the peak continues to grow while simultaneously shifting to a final value of 183 ppm during the sloping process 3′ (Figure 3b). This suggests that this process proceeds first via a two-phase reaction, then by a solid-solution reaction. In order to identify these structures, we performed refinements against multiple data sets from our *operando* PDF experiment. Initial refinements suggested three potential structures, all of which were able to match the PDF

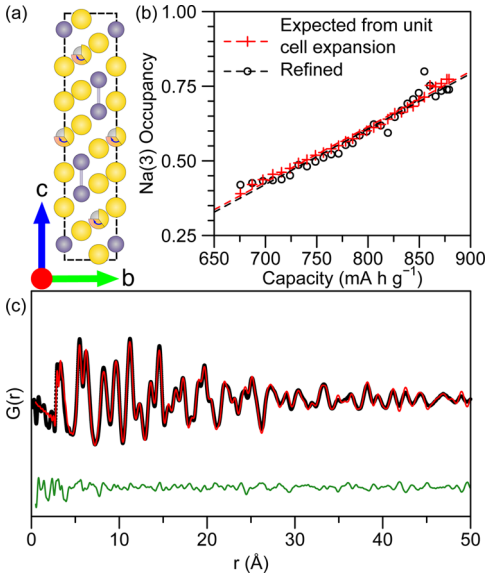

Figure 6. (a) A projection of the $Na_{5-x}Sn_2$ class of structures viewed down the *a*-axis. Sodium atoms are shown in yellow, tin in gray, the partial occupancies of the third sodium site are indicated increasing from 0.4 to 0.75 by blue arrows. (b) A plot of the occupancy of Na site 3 vs time spent on this electrochemical process. Occupancies derived directly from PDF refinements are shown as black circles, occupancies determined from the volume expansion of the crystal lattice (assuming an Na ionic radius of 1.10 Å) are shown as red crosses. Trends are indicated for both data series as dashed lines. (c) Fit of the PDF corresponding to the first frame obtained during this process over the range 0−50 Å (R_w = 0.19). Raw data are shown as black circles, the fit is shown as a red line, and the difference is shown as a green line offset below.

data well: Na_2Sn, Na_7Sn_3, and Na_5Sn_2 (R_w = 0.18, 0.18, and 0.19, respectively). These structures all belong to the $R\bar{3}m$ space group. The major difference between these three structures is the addition of a third sodium site in the Na_7Sn_3 and Na_5Sn_2 structures compared with the Na_2Sn structure (having an occupancy of 0.8 and 1, respectively), as highlighted in Figure 6a. While they all provide a good match in terms of a low residual, the latter two structures required higher values for the thermal displacement parameters (U_{iso}) of the sodium atoms. This suggests that the contribution of sodium correlations to the fitted PDF is being broadened in order to match the experimental data, implying the sodium positions and/or stoichiometry in the model structures is incorrect. Through refining the thermal displacement parameter for the third sodium site independently of the other two, it is apparent that the sodium in this site has a substantially higher value for U_{iso}, indicating that the refinement is seeking to disorder these sites; i.e., the models are likely incorrect. We performed further refinements based upon the Na_5Sn_2 structure, but allowing the occupancy of this site to vary. This revealed a linear increase in the occupancy during the sloping electrochemical process 3′ (Figure 6b), starting at a value of approximately 0.4 and ending at approximately 0.75. The occupancy may also be indirectly derived from the observed volume expansion of the crystal lattice: the rate of increase of occupancy is identical to that obtained through PDF refinements if an ionic radius for sodium of 1.10 Å is assumed. This is consistent with the sodium ions having a coordination number between 6 and 8.[46] An example of the fit to a measured PDF is given in Figure 6c. Full details of these calculations are given in the SI.

DOI: 10.1021/jacs.7b01398
J. Am. Chem. Soc. 2017, 139, 7273−7286

We, therefore, propose that this electrochemical process starts with the formation of $Na_{4.4}Sn_2$ during process 3 followed by a solid solution of structures of the form $Na_{5-x}Sn_2$ during process 3′, ending at $Na_{4.75}Sn_2$. This is also consistent with the observed slope in the electrochemistry during process 3′, which is typically indicative of solid-solution behavior.

Processes 4 and 4′. The final discharge product, $Na_{15}Sn_4$, is well-known in the literature.[4,7,17,47] We were not able to observe complete formation of this phase during our *operando* PDF measurement, which we believe was due to the increased resistance of the *operando* electrochemical cells. In addition, we were unable to hold the cell at the end of discharge for long enough to allow complete conversion owing to the limited amount of allocated beamtime; complete conversion was observed during the *operando* NMR measurement, however, owing to the greater amount of time spent holding the cell potential at 1 mV. *Ex situ* PDF measurements were able to confirm the formation of $Na_{15}Sn_4$, with no significant distortions from the average $Na_{15}Sn_4$ structure (SI). During our *operando* ^{23}Na NMR experiment, however, we observed the formation of peaks at both −75 and −260 ppm at the end of discharge. The peak at −75 ppm is observed to grow first, and is tentatively ascribed to the formation of $Na_{15}Sn_4$. This structure consists of isolated tin atoms within an expanse of sodium atoms; the incorporation of an excess of sodium within this crystal structure would not require further breaking of Sn−Sn bonds and could therefore be expected to be relatively facile. It is to this ($Na_{15+x}Sn_4$) that we tentatively assign the signal at −260 ppm. This is analogous to the processes by which $Li_{15+x}Si_4$ and $Li_{15+x}Ge_4$ form electrochemically.[35,48] It should be noted that, while $Na_{15}Sn_4$ contains two crystallographically distinct sodium sites, the differing rates of growth of these two peaks suggests they result from different phases. Upon reversal of the current, the peak at −260 ppm almost immediately vanishes, and is replaced with a broader resonance around −360 ppm, which quickly disappears. The peak at −75 ppm shrinks much more gradually throughout the entire electrochemical process. This behavior is identical to that seen in the lithium−silicon system.

Ex situ ^{119}Sn MAS ssNMR measurements for the material formed at the end of discharge (Figure S16) reveal two sharp peaks at 122 and 385 ppm. As $Na_{15}Sn_4$ only contains one crystallographic tin site, this is further evidence for the formation of an additional structurally related phase at the end of discharge.

Relaxation. In order to verify that the structures formed during the third electrochemical process are metastable as predicted by our calculations, we further performed some *in situ* ^{23}Na ssNMR experiments to observe how the structure relaxes upon removal of the applied current. We observe a continual shift and sharpening of the peak at 200 ppm formed upon discharge. This is a clear indication that the structure changes even without an applied current. During this time the measured potential is found to increase. The shift to higher frequencies is consistent with sodium removal from the structure, which is likely a result of reaction with the electrolyte or SEI. This would also be consistent with the increasing potential of the cell. While detailed diffraction measurements have yet to be performed in order to identify the structure(s) formed, we present this as evidence supporting the use of *operando* measurements for both this system and other, highly reactive, alloying materials. Further details are given in the SI.

DISCUSSION

Based on our PDF, XRD, ssNMR measurements and theoretical calculations, we propose the following discharge mechanism for the sodium−tin system:

- Process 1: Sn → $NaSn_3$
- Process 1′: Sn, $NaSn_3$ → $NaSn_2$
- Process 2: $NaSn_2$ → *a*-$Na_{1.2}Sn$
- Process 2′: *a*-$Na_{1.2}Sn$ + $NaSn_2$ → *a*-$Na_{1.2}Sn$ + expanded $Na_{1+x}Sn_2$ (solid solution)
- Process 3: *a*-$Na_{1.2}Sn$ + expanded $Na_{1+x}Sn_2$ → $Na_{4.4}Sn_2$
- Process 3′: $Na_{4.4}Sn_2$ → $Na_{4.75}Sn_2$ (solid solution)
- Process 4: $Na_{4.75}Sn_2$ → $Na_{15}Sn_4$
- Process 4′: $Na_{15}Sn_4$ → $Na_{15+x}Sn_4$

The first transformation (processes 1 and 1′) is from crystalline *β*-Sn to another crystalline material. This is in contrast to many alloying systems, notably sodium−antimony[5,43] and lithium−silicon,[49] where the first electrochemical process involves the formation of an amorphous structure due to the overpotential required to break up the crystalline lattice of the starting material. A transformation between two crystalline species without intermediate amorphization suggests a relatively facile transition, requiring only small changes in tin connectivity. This is readily observable in our *operando* PDF data, with only minor changes observed at low *r* (Figure 7a). These processes result in the conversion from *β*-Sn to a layered structure of composition $NaSn_2$ via an intermediate with a similar structure to $NaSn_2$ of approximate stoichiometry $NaSn_3$. Figure 7b,c demonstrates the similarity of the end-member structures, with significant short-range changes highlighted with colored lines.

NMR measurements of this phase reveal strongly Knight shifted features consistent with the likely electronic properties of the stanine-like tin layer. The slow convergence of the phonon spectra with respect to the k-point sampling, could also hint at a strong electron−phonon coupling and a complex Fermi surface shape. These properties are consistent with the structural similarities of this phase to structures such as MgB_2, which are studied in the context of high-temperature superconductors.[50] The full understanding of the electronic structure of $NaSn_2$ is, however, beyond the scope of this study.

The lower sodium-content phase, approximate composition $NaSn_3$, is almost identical to that of $NaSn_2$ noted earlier, but with a reduction in symmetry caused by the presence of tin atoms within the sodium layers. The formation of this additional intermediate implies that, while the breakup of *β*-Sn is relatively facile compared to other alloying systems, there is a preference to go via an additional structurally related intermediate ($NaSn_3$) rather than phase separate into the two end member phases, *β*-Sn and $NaSn_2$. It is possible that this may help to mediate strain at the interface between the two phases.

The second electrochemical process is kinetically driven, resulting primarily in the formation of an amorphous phase, rather than the thermodynamically stable NaSn. The high melting-point of the crystalline NaSn phase,[31] along with its low electrical conductivity, as observed by NMR, both point to low atomic mobility within the structure. This, combined with the large structural rearrangement that would be necessary to form Sn_4 clusters in the crystalline thermodynamic phase, is a likely reason for why it does not form. Qualitatively, the voltage curve obtained using the crystalline Na_1Sn_1 phase describes better the charge curve in this region (Figure 1b), whereas the

DOI: 10.1021/jacs.7b01398
J. Am. Chem. Soc. 2017, 139, 7273−7286

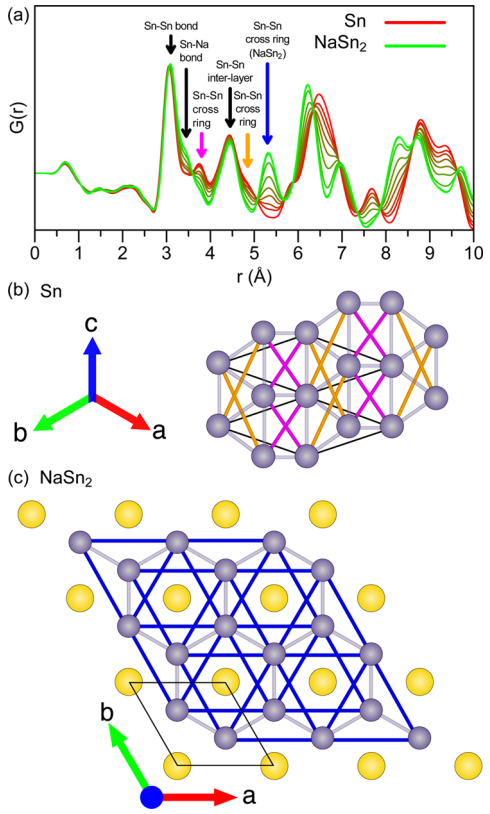

Figure 7. (a) PDFs obtained during an *operando* measurement corresponding to electrochemical processes 1 and 1′. The first scan during this process corresponds to *β*-Sn (red), the last to $NaSn_2$ (green). The cell was cycled at a rate of *C*/70 (corresponding to achieving the theoretical capacity in 70 h), and data were gathered at 2 h intervals. (b) A projection of the *β*-Sn structure viewed in the [111] direction. The short-range correlations lost during the structural transformation are indicated as orange and magenta lines, and are shown with the same color arrows in (a). (c) A projection of the $NaSn_2$ structure viewed down the *c*-axis. The short-range Sn−Sn correlations gained during the structural transformation are indicated with blue lines, and are shown with a blue arrow in (a). Tin atoms are shown in gray, sodium in yellow; Sn−Sn bonds are shown as gray lines.

discharge curve is better described by the amorphous Na_1Sn_1 phase; the much more well-defined plateaus during charging also being suggestive of the formation of a more ordered structure. During charging (sodium removal), the relative mobility of Na^+ ions and the need only to make rather than break bonds may make formation of a crystalline structure more favorable. This may explain the better representation of the charge curve by the crystalline Na_1Sn_1, and is suggestive that the mechanism for sodium removal may differ from that of sodium insertion contrary to previous reports.[7,17]

The tin connectivity in the amorphous phase primarily consists of chains of tin atoms, likely a consequence of the fact that it forms from the layered $NaSn_2$ phase. Despite this, we observed a clear tendency toward a small amount of tetrahedral connectivity, which is present in the thermodynamically stable crystalline NaSn phase. This indicates that the transformation is not exclusively kinetically driven, and the relative concentrations of the different species in the amorphous phase are likely rate dependent. In this region, we additionally observe some expansion and disordering in the interlayer direction of the $NaSn_2$ structure, indicating that addition of sodium between the layers of $NaSn_2$ might be kinetically more facile than breaking up the extended lattice. This is not unexpected owing to the ability of other layered materials (notably graphite) to swell and, ultimately, exfoliate electrochemically.[45]

At sodium concentrations higher than Na_2Sn, structures based upon tin dumbbells are formed. Our DFT calculations predict numerous dumbbell phases at similar energies, similar behavior also having been observed for a number of other chemically related systems.[34,35] It is clear that the structures formed experimentally during these process are very similar to Na_2Sn, Na_7Sn_3, and Na_5Sn_2—three structures that differ primarily through the occupancy of one of their sodium sites. The occupancy of this site was found (via refinement of the site occupancy) to increase linearly throughout the sloping electrochemical process 3′, thus providing an explanation for the solid-solution behavior implied by the electrochemistry. The addition of further sodium to the existing phase, rather than the immediate nucleation of $Na_{15}Sn_4$, is once again kinetically driven. The presence of a number of related structures at similar energies allows for a relatively facile transition between them simply through adding additional sodium atoms between the dumbbells. Conversely breaking up the tin dumbbells requires a greater input of energy. This result implies metastability of the structures produced during these processes. A further consequence of this may be that the structures formed may be different upon discharge and charge, as well as relaxation effects upon removal of the current; our preliminary data indicate that this is indeed the case and will be the subject of future work. A full analysis of the sodium removal mechanism is beyond the scope of this paper.

Given the number of apparently flat plateaus in the electrochemical profile, along with the relatively high number of crystalline intermediates, it may appear at first glance that the Na−Sn system is thermodynamically driven. The calculated voltage curve obtained from the structures predicted to be stable in DFT calculations matches the experimental curve fairly well, demonstrating the predictive capability of the theoretical methods used. The disagreement between the theoretical and experimental voltages (as shown by the difference between the blue and black lines in Figure 1b) can be attributed mainly to experimental effects such as finite particle size, surface, and kinetic effects including overpotentials, which are not included in the modeling. From our experimental data, it is also clear that kinetic considerations are very important to the transformations taking place, and understanding these additional complexities is necessary in order to understand the complex electrochemical behavior of the system. We note that the behavior during the kinetically driven regions is likely to be highly dependent on the overpotential at which the cell operates. This can be affected by electrode formulation, charge rate, and experimental setup, among other things, and can explain differences between the electrochemistry presented here and in other studies, most notably in thin films. These differences are also important to understand in the context of binary and ternary alloys with tin as a component, as the presence of additional inactive matrices, other active elements, and interfaces between nanosized regions is likely to have an effect on the kinetic pathways taken. For these electrodes to be implemented in practical systems, a full understanding of these processes as a function of experimental details such as rate and electrode formulation will be required.

DOI: 10.1021/jacs.7b01398
J. Am. Chem. Soc. 2017, 139, 7273−7286

CONCLUSIONS

We have successfully utilized the method of AIRSS + atomic species swapping in order to predict a variety of stable and locally stable structures. Using this theoretical framework, we were able to fully model our *operando* PDF and XRD data, which, combined with information from *operando* ssNMR measurements, provide a comprehensive understanding of the sodium−tin electrochemical system. Having access to the possible metastable structures can be very insightful when studying electrochemical processes, since these might occur far from equilibrium.

Experimental evidence for the formation of $NaSn_2$ during the first electrochemical processes, a phase predicted by our DFT calculations to be thermodynamically stable is presented. The results represent the first structural evidence that these processes result in the formation of two phases (the other being of approximate composition $NaSn_3$, which bears a strong similarity to $NaSn_2$, with the addition of tin atoms within the sodium layers).

Reverse Monte Carlo refinements against models produced by *ab initio* molecular dynamics were able to extract structural information about the amorphous intermediate formed during the second process, constraining the simulations with information from *operando* PDF measurements. The resulting model consists primarily of chains of tin atoms, and is consistent will all known experimental data on this phase. ^{119}Sn MAS ssNMR measurements were used to examine the connectivity present in the amorphous sodium−tin phases, with the value of the shift being found to be highly dependent upon the tin−tin connectivity. The relative concentration of each connectivity was shown to support the MD/RMC model.

Operando ssNMR data presented evidence for a solid-solution process during the process around 60 mV (labeled 3′). Detailed PDF refinements revealed an increase in occupancy of a single sodium site in dumbbell structures of the form $Na_{5-x}Sn_2$. Furthermore, our NMR data reveal, for the first time, the possibility of further sodium storage within the $Na_{15}Sn_4$ structure, formed toward the end of discharge, as an off-stoichiometry phase $Na_{15+x}Sn_4$, in a process analogous to that observed in the lithium−silicon system.

The first evidence for significant solid solution behavior and resulting metastability in the sodium−tin system is presented. The study provides a clear demonstration of the need for a variety of techniques probing both short- and long-range structures, along with a detailed theoretical underpinning of model structures, in order to comprehensively understand the mechanism of sodium insertion. Our results have further implications beyond the sodium−tin system, highlighting the fact that even a system under apparent thermodynamic control, the nature of electrochemical alloying means that kinetic considerations remain very important.

EXPERIMENTAL METHODS

Except were otherwise stated, all experiments were performed under ambient conditions.

Electrode Preparation. Tin powder (Sigma-Aldrich, ≥99%, particle size ≤150 nm), carbon Super P (Timcal), and sodium carboxymethyl cellulose (Sigma-Aldrich, DS = 0.7, M_w = 700 000) (70:19:11) were ball-milled in a water:ethanol solvent (70:30) using a SPEX 8000M mixer/mill for 15 min. The resulting viscous slurry was cast onto Mylar foil using a 300 μm doctor blade, dried for 16 h in air, and then a further 4 h at 100 °C *in vacuo*. The resultant self-supporting films were used for all the electrochemical measurements reported here.

Electrochemical experiments. Cells were prepared under an argon atmosphere using metallic sodium (Sigma-Aldrich, 99.9%) as an anode. The electrolyte was 1 M $NaPF_6$ (Alfa Aesar, ≥99%) in propylene carbonate (Sigma-Aldrich, anhydrous), and the separator was borosilicate glass fiber (Whatman, GF/A). *Ex situ* electrochemical measurements were performed with standard 2032 coin cell parts using a Biologic MPG2 battery cycler.

While commercial electrodes are usually fabricated by casting a slurry onto a metallic current collector (typically aluminum for sodium-ion batteries), the presence of such a current collector does not allow *operando* PDF and NMR measurements to be performed. In the case of PDF, the inhomogeneity caused by rolling the metal foil causes inconsistencies in the background depending upon where the beam hits. For NMR the metal foil shields the RF radiation, attenuating the signal. As such, all reported electrochemical data in this paper was performed using the self-supporting films described above. In order to maximize signal-to-noise for our measurements, films of greater thickness than are often used in electrochemistry measurements were also used (typically around 300 μm). Such films, if optimized are, in principle, of commercial relevance as they maximize the energy density that can be obtained without using large quantities of an expensive current collector. Increasing the thickness necessitated a corresponding increase in the temperature at which the cells were cycled in order to achieve an acceptable rate performance. We note no significant differences to the features observed in reported electrochemical measurements as a result of these changes, aside from additional capacity above 0.5 V, which we attribute to a combination of SnO on the surface of the nanoparticles, and additional electrolyte breakdown as a result of the large surface area exposed.

PDF Analysis. *Operando* PDF measurements were performed at beamline I15 at Diamond Light Source using a modified Swagelok cell adapted for X-ray transmission. Cells were prepared in an argon atmosphere glovebox (O_2, H_2O < 0.1 ppm) using the same materials as for the coin cell measurements. Electrochemical measurements were performed using an Ivium-n-Stat battery cycler. Cells were galvanostatically cycled in the potential range 2−0.001 V at a rate of $C/30$ (based on the mass of tin, corresponding to 3.75 Na per Sn in 30 h) and held at the end of discharge for the remainder of the experiment (a further 32 h).

Measurements were taken using an X-ray beam of energy 76 keV (λ = 0.1631 Å) and an amorphous silicon area detector (PerkinElmer) in order to gather data to large values of momentum transfer.[51,52] Data were collected at 60 min intervals, using a total exposure time of 60 s per scan.

Additional *operando* PDF and XRD measurements were performed at beamline 11-ID-B at the Advanced Photon Source, Argonne National Laboratory using the AMPIX cell.[53] Cells were prepared in an argon atmosphere glovebox (O_2, H_2O < 0.1 ppm) using the same materials as for the coin cell measurements. Electrochemical measurements were performed using a Maccor 4300 battery cycler. Cells were galvanostatically cycled in the potential range 2−0.001 V at a rate of $C/70$ (based on the mass of tin, corresponding to 3.75 Na per Sn in 70 h).

Measurements were taken using an X-ray beam of energy 86.7 keV (λ = 0.1430 Å) and an amorphous silicon area detector (PerkinElmer) in order to gather data to large values of momentum transfer.[51,52] Data were collected at 60 min intervals, alternating diffraction mode and PDF mode using an exposure time of 300 s at a temperature of 60 °C.

For all PDF and XRD experiments, background measurements were taken using identical cells, but without the active material present. A CeO_2 standard was used to determine the sample geometry and the sample-to-detector distance. The data were converted to a function of intensity vs Q using FIT2D or Data Analysis WorkbeNch (DAWN).[54,55] Standard corrections (background, Compton scattering, detector effects) were applied, and the data were Fourier transformed to obtain $G(r)$ using the software PDFGetX2.[56] Structural refinements were performed on the crystalline components using

DOI: 10.1021/jacs.7b01398
J. Am. Chem. Soc. 2017, 139, 7273−7286

PDFGUI.[57] Reverse Monte Carlo refinements were performed using RMCProfile.[58]

Solid-State NMR Spectroscopy. In-house designed cells based upon a cylindrical capsule[59] were prepared in an argon atmosphere glovebox (O_2, H_2O < 0.1 ppm) using the same materials as for the coin cell measurements. Electrochemical measurements were performed using a Bio-Logic VSP battery cycler. Cells were galvanostatically cycled in the potential range 2−0.001 V at a rate of *C*/30 (based on the mass of tin, corresponding to 3.75 Na per Sn in 30 h), and held at 1 mV until the applied current dropped to *C*/100, which ensures complete reaction of the electrode materials (a process commonly required for *operando* measurements, where there is an increased resistance of the electrochemical cell caused by modifications to the cell design to allow external monitoring—by radio frequency fields in this case).[48] Cells were cycled at a temperature of 35 °C.

Operando ssNMR measurements were performed using a Bruker Avance 300 MHz spectrometer (^{23}Na Larmor frequency = 79.39 MHz). It was observed that the formation of intermetallic species during operation of the batteries radically changed the required tuning and matching parameters. Using a conventional static probe, with a resonance circuit fixed at the start of the experiment, thus resulted in a reduction in the quality of data gathered as the properties of the electrodes changed. In order to overcome these difficulties, a static probe system with automatic tuning and matching capabilities (along with connections for an external battery cycler) was used.[60] The resonance circuit was recalibrated immediately prior to each measurement by minimizing the standing wave ratio of the forward and reflected power for a low-power (0.01 W) continuous-wave pulse. The electrochemical cell was aligned such that the electrodes were perpendicular to the applied field.

In order to maximize the signal-to-noise ratio for a time-restricted measurement, a one-pulse sequence was used. A 90° pulse corresponded to 4.5 μs at 200 W using an 11 mm diameter silver coil. 25600 transients were collected for each spectrum, using a recycle delay of 0.05 s (30 min per spectrum). The ^{23}Na signals were referenced using a 1 M solution of NaCl at a shift of 0 ppm.[61] Spectra were Fourier transformed and individually phased using Bruker Topspin 3.2. Backgrounds were subtracted using fityk.[62]

Ex situ ^{23}Na magic angle spinning (MAS) ssNMR measurements were performed using a Bruker Avance III 200 MHz spectrometer (^{23}Na and ^{119}Sn Larmor frequencies of 52.92 and 74.61 MHz, respectively). 1.3 mm zirconia rotors were spun at 60 kHz using a Bruker double-resonance probehead. For the ^{23}Na measurements, a MAS speed synchronized Hahn-echo pulse sequence with 90−180° pulses corresponding to 2−4 μs at 25 W was applied, and a recycle delay of 0.05 s was used. Spectra were referenced using NaCl powder at 7.21 ppm.[63] For the ^{119}Sn measurements, a Hahn-echo pulse sequence with 90−180° pulses corresponding to 1.38−2.76 μs at 43.5 W was applied, and a recycle delay of 0.3 s was used. Spectra were referenced using SnO_2 powder at −604.3 ppm.[64]

Samples for *ex situ* MAS NMR investigations were prepared electrochemically; cells were cycled at a rate of *C*/20 (based on the mass of tin, corresponding to 3.75 Na per Sn in 20 h) to the point of interest on the electrochemical curve at a temperature of 55 °C. The electrodes were recovered inside an argon atmosphere glovebox (O_2, H_2O < 0.1 ppm), washed with dimethylcarbonate (Sigma-Aldrich, anhydrous, >99%), and immediately dried *in vacuo*. The respective electrode films were then individually ground and packed into rotors immediately. Decomposition was minimized by careful and rapid handling of the materials within a glovebox. However, the samples were found to degrade in under 5 min of exposure to the glovebox atmosphere, so it is possible that small quantities of decomposition products remain.

Structure Prediction. The structure prediction was performed using AIRSS.[21] Within the AIRSS method, random structures are generated and then relaxed to a local minimum in the potential energy surface (PES) using DFT forces. The large number of relaxed structures generated enables wide coverage of the PES of the system. Based on general physical principles and system-specific constraints, the search can be biased in a variety of sensible ways.[22] The AIRSS search was complemented with a high-throughput screening from the ICSD.[16] All combinations of {Li,Na,K}−{Si,Ge,Sn,Pb} crystal structures at different stoichiometries were obtained from the ICSD. For each structure, the anions and cations were swapped to Na and Sn, respectively, and then relaxed using DFT forces. The AIRSS + species swapping method been successfully used for Li−Si,[34] Li−Ge,[34,35] Li−S,[65] and Li−P[66] systems. Furthermore, a study on point defects in silicon has been presented using the AIRSS method.[67]

Approximately 4000 structures were generated by AIRSS. We found the energetics of the system hard to converge using low-accuracy pseudopotentials usually used in our high-throughput studies which limited the amount of random structures generated by our search. The calculations were performed using the CASTEP DFT plane-wave code[68] using the gradient corrected Perdew−Burke−Ernzerhof (PBE) exchange-correlation functional. The core electrons were described using Vanderbilt "ultrasoft" pseudopotentials.[69] For the initial AIRSS searches, the Brillouin zone (BZ) was sampled using a Monkhorst−Pack[70] grid with a k-point spacing finer than $2\pi \times 0.05$ Å^{-1}, and the plane wave basis set was truncated at an energy cutoff value of 500 eV. The low-energy structures obtained by the search were refined with higher accuracy using a k-point spacing finer than $2\pi \times 0.03$ Å^{-1} and an energy cutoff of 800 eV along with more accurate pseudopotentials.[71] This level of accuracy was used to calculate all properties throughout this study, unless stated otherwise. The structures obtained from the ICSD were relaxed with the same level of theory.

The system's thermodynamical phase stability was assessed by comparing the free energy of different phases. From the obtained DFT total energy, $E\{A_aB_b\}$, of a given binary phase of elements A and B with stoichiometry A_aB_b, a formation energy per atom was defined as

$$E_f/\text{atom} = \frac{E\{A_aB_b\} - aE\{A\} - bE\{B\}}{a+b} \quad (1)$$

The formation energies of each structure were plotted as a function of the A element concentration, $u = a/(a+b)$, starting at $u = 0$ and ending at $u = 1$. A convex hull was constructed between the chemical potentials at $(u, E_f/\text{atom}) = (0, 0)$ and $(1, 0)$ by drawing a tie-line that joins the lowest energy structures. This construction gives access to the 0 K stable structure since the second law of thermodynamics demands that the (free) energy per atom is a convex function of the relative concentrations of the atoms (see Figure 1a). A more detailed description of the convex hull construction may be found in ref 34.

Average voltages for the structures lying on the hull were calculated from the available DFT total energies. For two given phases on the hull, $A_{x_1}B$ and $A_{x_2}B$, with $x_2 > x_1$, the following two-phase reaction is assumed:

$$A_{x_1}B + (x_2 - x_1)A \rightarrow A_{x_2}B \quad (2)$$

The voltage, *V*, is given by[72]

$$V = -\frac{\Delta G}{x_2 - x_1} \approx -\frac{\Delta E}{x_2 - x_1} = -\frac{E(A_{x_2}B) - E(A_{x_1}B)}{x_2 - x_1} + E(A) \quad (3)$$

where it is assumed that the Gibbs energy can be approximated by the internal energy, as the *pV* and thermal energy contributions are small.[72]

Phonon dispersion curves were calculated using density-functional perturbation theory in CASTEP.[28] Norm-conserving pseudopotentials were used, the Brillouin zone was sampled using a Monkhorst−Pack grid with a *k*-point spacing finer than $2\pi \times 0.0175$ Å^{-1}, and the plane wave basis set was truncated at an energy cutoff of 1200 eV.[70] The structures were fully relaxed at this level of accuracy.

Born−Oppenheimer molecular dynamics (BOMD) simulations were run in CASTEP using an NVT ensemble using a Nosé−Hoover thermostat,[73] a 1 fs integration time step, "ultrasoft" pseudopotentials, a planewave cutoff energy of 500 eV, and with integrals taken over the Γ point. Initially, a 64 atom cubic supercell with composition Na_1Sn_1 was created by placing the atoms in random positions obeying the density and minimum atomic distances found in Na_1Sn_1−$I4_1/acd$. The

DOI: 10.1021/jacs.7b01398
J. Am. Chem. Soc. 2017, 139, 7273−7286

system was heated to 1000 K at 1 K/fs, equilibrated during 3 ps, cooled at rate of 1 K/fs to 300 K, and equilibrated for 4 ps; finally, the atomic configurations were sampled over the last 5 ps. The sampled atomic configurations were averaged, and the resulting structure was relaxed using the same level of theory used in the convex hull construction.

■ ASSOCIATED CONTENT

Supporting Information

The Supporting Information is available free of charge on the ACS Publications website at DOI: 10.1021/jacs.7b01398.

Further details about DFT calculations and electrochemistry, PDF, XRD, and NMR measurements, including Tables S1−S7 and Figures S1−S22 (PDF)

■ AUTHOR INFORMATION

Corresponding Authors

*ajm255@cam.ac.uk

*cpg27@cam.ac.uk

ORCID

Joshua M. Stratford: 0000-0002-6867-4226

Martin Mayo: 0000-0001-5761-6736

Clare P. Grey: 0000-0001-5572-192X

Notes

The authors declare no competing financial interest.

Additional data related to this publication are available at the Cambridge data repository https://doi.org/10.17863/CAM.7653

■ ACKNOWLEDGMENTS

The authors thank Dr. Karen Johnston, Dr. Nicole Trease, Dr. Matthew Cliffe, and Dr. John Griffin for useful discussions. Dr. Peter Chupas, Dr. Annette Kleppe, Dr. Philip Chater, and Dr. Maria Tsiamtsouri are gratefully thanked for their assistance in running the PDF measurements. This research used resources of the Advanced Photon Source, a U.S. Department of Energy (DOE) Office of Science User Facility operated for the DOE Office of Science by Argonne National Laboratory under Contract no. DE-AC02-06CH11357. We thank Diamond Light Source for the provision of beamtime on I15 (EE13681) that contributed to the results presented here. This work was supported by STFCBatteries.org through the STFC Futures Early Career Award (J.M.S.). J.M.S. acknowledges funding from the Assistant Secretary for Energy Efficiency and Renewable Energy, Office of Vehicle Technologies, of the U.S. DOE under Contract no. DE-AC02-05CH11231, under the Batteries for Advanced Transportation Technologies (BATT) Program subcontract no. 7057154, and the European Commission under grant agreement no. 696656 (Graphene Flagship). P.K.A. acknowledges the School of the Physical Sciences of the University of Cambridge for funding through an Oppenheimer Research Fellowship and a Junior Research Fellowship from Gonville and Caius College, Cambridge. This project has received funding from the European Union's Horizon 2020 research and innovation programme under the Marie Skłodowska-Curie grant agreement no. 655444 (O.P.). M.M. and A.J.M. acknowledge the support from the Winton Programme for the Physics of Sustainability. A.J.M. and C.J.P. were supported by Engineering and Physical Sciences Research Council (EPSRC) of the United Kingdom (Grant no. EP/G007489/2). C.J.P. is also supported by the Royal Society through a Royal Society Wolfson Research Merit award. Calculations were performed using the Archer facility of the UK national high performance computing service, for which access was obtained via the UKCP consortium and funded by EPSRC grant no. EP/K014560/1.

■ REFERENCES

(1) Ponrouch, A.; Monti, D.; Boschin, A.; Steen, B.; Johansson, P.; Palacín, M. R. *J. Mater. Chem. A* **2015**, *3*, 22−42.

(2) Kim, S.-W.; Seo, D.-H.; Ma, X.; Ceder, G.; Kang, K. *Adv. Energy Mater.* **2012**, *2*, 710−721.

(3) Chevrier, V. L.; Ceder, G. *J. Electrochem. Soc.* **2011**, *158*, A1011−A1014.

(4) Komaba, S.; Matsuura, Y.; Ishikawa, T.; Yabuuchi, N.; Murata, W.; Kuze, S. *Electrochem. Commun.* **2012**, *21*, 65−68.

(5) Darwiche, A.; Marino, C.; Sougrati, M. T.; Fraisse, B.; Stievano, L.; Monconduit, L. *J. Am. Chem. Soc.* **2012**, *134*, 20805−20811.

(6) Baggetto, L.; Keum, J. K.; Browning, J. F.; Veith, G. M. *Electrochem. Commun.* **2013**, *34*, 41−44.

(7) Baggetto, L.; Ganesh, P.; Meisner, R. P.; Unocic, R. R.; Jumas, J.-C.; Bridges, C. A.; Veith, G. M. *J. Power Sources* **2013**, *234*, 48−59.

(8) Xiao, L.; Cao, Y.; Xiao, J.; Wang, W.; Kovarik, L.; Nie, Z.; Liu, J. *Chem. Commun.* **2012**, *48*, 3321−3323.

(9) Zhou, D.; Slater, M.; Kim, D.; Lee, E.; Jorne, J.; Johnson, C. *ECS Trans.* **2014**, *58*, 59−64.

(10) Wu, L.; Hu, X.; Qian, J.; Pei, F.; Wu, F.; Mao, R.; Ai, X.; Yang, H.; Cao, Y. *J. Mater. Chem. A* **2013**, *1*, 7181−7184.

(11) Prikhodchenko, P. V.; Yu, D. Y. W.; Batabyal, S. K.; Uvarov, V.; Gun, J.; Sladkevich, S.; Mikhaylov, A. A.; Medvedev, A. G.; Lev, O. *J. Mater. Chem. A* **2014**, *2*, 8431−8437.

(12) Zhu, J.; Deng, D. *J. Phys. Chem. C* **2015**, *119*, 21323−21328.

(13) Kremann, R.; Gmachl-Pammer, J. *Z. Metallkd.* **1920**, *12*, 257.

(14) Crouch-Baker, S.; Deublein, G.; Tsai, H.-C.; Zhou, L. Z.; Huggins, R. A. *Solid State Ionics* **1990**, *42*, 109−115.

(15) Inoue, T.; Saito, M.; Fujimoto, M.; Itaya, M. Sodium ion secondary battery. U.S. Patent Application 20070218361, 2007.

(16) Inorganic Crystal Structure Database, icsd.fiz-karlsruhe.de (accessed Jan 31, 2017).

(17) Ellis, L. D.; Hatchard, T. D.; Obrovac, M. N. *J. Electrochem. Soc.* **2012**, *159*, A1801−A1805.

(18) Wang, J. W.; Liu, X. H.; Mao, S. X.; Huang, J. Y. *Nano Lett.* **2012**, *12*, 5897−5902.

(19) Li, Z.; Ding, J.; Mitlin, D. *Acc. Chem. Res.* **2015**, *48*, 1657−1665.

(20) Baggetto, L.; Bridges, C. A.; Jumas, J.-C.; Mullins, D. R.; Carroll, K. J.; Meisner, R. A.; Crumlin, E. J.; Liu, X.; Yang, W.; Veith, G. M. *J. Mater. Chem. A* **2014**, *2*, 18959−18973.

(21) Pickard, C. J.; Needs, R. J. *Phys. Rev. Lett.* **2006**, *97*, 045504.

(22) Pickard, C. J.; Needs, R. J. *J. Phys.: Condens. Matter* **2011**, *23*, 053201.

(23) Fässler, T. F.; Kronseder, C. *Angew. Chem., Int. Ed.* **1998**, *37*, 1571−1575.

(24) Fässler, T. F.; Hoffmann, S. *Inorg. Chem.* **2003**, *42*, 5474−5476.

(25) Müller, W.; Volk, K. *Z. Naturforsch., B: J. Chem. Sci.* **1977**, *32*, 709−710.

(26) Müller, W.; Volk, K. *Z. Naturforsch., B: J. Chem. Sci.* **1975**, *30*, 494−496.

(27) Dubois, F.; Schreyer, M.; Fässler, T. F. *Inorg. Chem.* **2005**, *44*, 477−479.

(28) Refson, K.; Tulip, P. R.; Clark, S. J. *Phys. Rev. B: Condens. Matter Mater. Phys.* **2006**, *73*, 155114.

(29) Shao, J.; Beaufils, C.; Kolmogorov, A. N. *Sci. Rep.* **2016**, *6*, 28369.

(30) Beekman, M.; Nenghabi, E. N.; Biswas, K.; Myles, C. W.; Baitinger, M.; Grin, Y.; Nolas, G. S. *Inorg. Chem.* **2010**, *49*, 5338−5340.

(31) Sangster, J.; Bale, C. W. *J. Phase Equilib. Diffus.* **1998**, *19*, 76−81.

(32) Vaughey, J. T.; Corbett, J. D. *Inorg. Chem.* **1997**, *36*, 4316−4320.

DOI: 10.1021/jacs.7b01398
J. Am. Chem. Soc. 2017, 139, 7273−7286

(33) Müller, W.; Volk, K. *Z. Naturforsch., B: J. Chem. Sci.* **1978**, *33*, 275−278.
(34) Morris, A. J.; Grey, C. P.; Pickard, C. J. *Phys. Rev. B: Condens. Matter Mater. Phys.* **2014**, *90*, 054111.
(35) Jung, H.; Allan, P. K.; Hu, Y.-Y.; Borkiewicz, O. J.; Wang, X.-L.; Han, W.-Q.; Du, L.-S.; Pickard, C. J.; Chupas, P. J.; Chapman, K. W.; Morris, A. J.; Grey, C. P. *Chem. Mater.* **2015**, *27*, 1031−1041.
(36) Trease, N. M.; Zhou, L.; Chang, H. J.; Zhu, B. Y.; Grey, C. P. *Solid State Nucl. Magn. Reson.* **2012**, *42*, 62−70.
(37) Slater, M. D.; Kim, D.; Lee, E.; Johnson, C. S. *Adv. Funct. Mater.* **2013**, *23*, 947−958.
(38) Stevens, D. A.; Dahn, J. R. *J. Electrochem. Soc.* **2001**, *148*, A803−A811.
(39) Su, D.; Xie, X.; Wang, G. *Chem. - Eur. J.* **2014**, *20*, 3192−3197.
(40) Wang, Y.-X.; Lim, Y.-G.; Park, M.-S.; Chou, S.-L.; Kim, J. H.; Liu, H.-K.; Dou, S.-X.; Kim, Y.-J. *J. Mater. Chem. A* **2014**, *2*, 529−534.
(41) Klösters, G.; Jansen, M. *Solid State Nucl. Magn. Reson.* **2000**, *16*, 279−283.
(42) Basu, S.; Zeller, C.; Flanders, P. J.; Fuerst, C. D.; Johnson, W. D.; Fischer, J. E. *Mater. Sci. Eng.* **1979**, *38*, 275−283.
(43) Allan, P. K.; Griffin, J. M.; Darwiche, A.; Borkiewicz, O. J.; Wiaderek, K. M.; Chapman, K. W.; Morris, A. J.; Chupas, P. J.; Monconduit, L.; Grey, C. P. *J. Am. Chem. Soc.* **2016**, *138*, 2352−2365.
(44) Wiaderek, K. M.; Borkiewicz, O. J.; Castillo-Martínez, E.; Robert, R.; Pereira, N.; Amatucci, G. G.; Grey, C. P.; Chupas, P. J.; Chapman, K. W. *J. Am. Chem. Soc.* **2013**, *135*, 4070−4078.
(45) Lu, J.; Yang, J.; Wang, J.; Lim, A.; Wang, S.; Loh, K. P. *ACS Nano* **2009**, *3*, 2367−2375.
(46) Shannon, R. D. *Acta Crystallogr., Sect. A: Cryst. Phys., Diffr., Theor. Gen. Crystallogr.* **1976**, *32*, 751−767.
(47) Nam, D.-H.; Hong, K.-S.; Lim, S.-J.; Kim, T.-H.; Kwon, H.-S. *J. Phys. Chem. C* **2014**, *118*, 20086−20093.
(48) Ogata, K.; Salager, E.; Kerr, C. J.; Fraser, A. E.; Ducati, C.; Morris, A. J.; Hofmann, S.; Grey, C. P. *Nat. Commun.* **2014**, *5*, 3217.
(49) Key, B.; Morcrette, M.; Tarascon, J.-M.; Grey, C. P. *J. Am. Chem. Soc.* **2011**, *133*, 503−512.
(50) Choi, H. J.; Roundy, D.; Sun, H.; Cohen, M. L.; Louie, S. G. *Nature* **2002**, *418*, 758−760.
(51) Chupas, P. J.; Qiu, X.; Hanson, J. C.; Lee, P. L.; Grey, C. P.; Billinge, S. J. L. *J. Appl. Crystallogr.* **2003**, *36*, 1342−1347.
(52) Chupas, P. J.; Chapman, K. W.; Lee, P. L. *J. Appl. Crystallogr.* **2007**, *40*, 463−470.
(53) Borkiewicz, O. J.; Shyam, B.; Wiaderek, K. M.; Kurtz, C.; Chupas, P. J.; Chapman, K. W. *J. Appl. Crystallogr.* **2012**, *45*, 1261−1269.
(54) Hammersley, A. P.; Svensson, S. O.; Hanfland, M.; Fitch, A. N.; Hausermann, D. *High Pressure Res.* **1996**, *14*, 235−248.
(55) Basham, M.; Filik, J.; Wharmby, M. T.; Chang, P. C. Y.; El Kassaby, B.; Gerring, M.; Aishima, J.; Levik, K.; Pulford, B. C. A.; Sikharulidze, I.; Sneddon, D.; Webber, M.; Dhesi, S. S.; Maccherozzi, F.; Svensson, O.; Brockhauser, S.; Náray, G.; Ashton, A. W. *J. Synchrotron Radiat.* **2015**, *22*, 853−858.
(56) Qiu, X.; Thompson, J. W.; Billinge, S. J. L. *J. Appl. Crystallogr.* **2004**, *37*, 678.
(57) Farrow, C. L.; Juhas, P.; Liu, J. W.; Bryndin, D.; Božin, E. S.; Bloch, J.; Proffen, T.; Billinge, S. J. L. *J. Phys.: Condens. Matter* **2007**, *19*, 335219.
(58) Tucker, M. G.; Keen, D. A.; Dove, M. T.; Goodwin, A. L.; Hui, Q. *J. Phys.: Condens. Matter* **2007**, *19*, 335218.
(59) Pecher, O.; Carretero-González, J.; Griffith, K. J.; Grey, C. P. *Chem. Mater.* **2017**, *29*, 213−242.
(60) Pecher, O.; Bayley, P. M.; Liu, H.; Liu, Z.; Trease, N. M.; Grey, C. P. *J. Magn. Reson.* **2016**, *265*, 200−209.
(61) Harris, R. K.; Becker, E. D. *J. Magn. Reson.* **2002**, *156*, 323−326.
(62) Wojdyr, M. *J. Appl. Crystallogr.* **2010**, *43*, 1126−1128.
(63) Hayashi, S.; Hayamizu, K. *Bull. Chem. Soc. Jpn.* **1989**, *62*, 2429−2430.
(64) Clayden, N. J.; Dobson, C. M.; Fern, A. *J. Chem. Soc., Dalton Trans.* **1989**, *5*, 843−847.
(65) See, K. A.; Leskes, M.; Griffin, J. M.; Britto, S.; Matthews, P. D.; Emly, A.; Van Der Ven, A.; Wright, D. S.; Morris, A. J.; Grey, C. P.; Seshadri, R. *J. Am. Chem. Soc.* **2014**, *136*, 16368−16377.
(66) Mayo, M.; Griffith, K. J.; Pickard, C. J.; Morris, A. J. *Chem. Mater.* **2016**, *28*, 2011−2021.
(67) Morris, A. J.; Needs, R. J.; Salager, E.; Grey, C. P.; Pickard, C. J. *Phys. Rev. B: Condens. Matter Mater. Phys.* **2013**, *87*, 174108.
(68) Clark, S. J.; Segall, M. D.; Pickard, C. J.; Hasnip, P. J.; Probert, M. I. J.; Refson, K.; Payne, M. C. *Z. Kristallogr. - Cryst. Mater.* **2005**, *220*, 567−570.
(69) Perdew, J. P.; Burke, K.; Ernzerhof, M. *Phys. Rev. Lett.* **1996**, *77*, 3865−3868.
(70) Monkhorst, H. J.; Pack, J. D. *Phys. Rev. B* **1976**, *13*, 5188−5192.
(71) Lejaeghere, K.; Bihlmayer, G.; Bjorkman, T.; Blaha, P.; Blugel, S.; Blum, V.; Caliste, D.; Castelli, I. E.; Clark, S. J.; Dal Corso, A.; de Gironcoli, S.; Deutsch, T.; Dewhurst, J. K.; Di Marco, I.; Draxl, C.; Dułak, M.; Eriksson, O.; Flores-Livas, J. A.; Garrity, K. F.; Genovese, L.; Giannozzi, P.; Giantomassi, M.; Goedecker, S.; Gonze, X.; Grånäs, O.; Gross, E. K. U.; Gulans, A.; Gygi, F.; Hamann, D. R.; Hasnip, P. J.; Holzwarth, N. A. W.; Iuşan, D.; Jochym, D. B.; Jollet, F.; Jones, D.; Kresse, G.; Koepernik, K.; Küçükbenli, E.; Kvashnin, Y. O.; Locht, I. L. M.; Lubeck, S.; Marsman, M.; Marzari, N.; Nitzsche, U.; Nordström, L.; Ozaki, T.; Paulatto, L.; Pickard, C. J.; Poelmans, W.; Probert, M. I. J.; Refson, K.; Richter, M.; Rignanese, G.-M.; Saha, S.; Scheffler, M.; Schlipf, M.; Schwarz, K.; Sharma, S.; Tavazza, F.; Thunström, P.; Tkatchenko, A.; Torrent, M.; Vanderbilt, D.; van Setten, M. J.; Van Speybroeck, V.; Wills, J. M.; Yates, J. R.; Zhang, G.-X.; Cottenier, S. *Science* **2016**, *351*, aad3000.
(72) Aydinol, M. K.; Kohan, A. F.; Ceder, G.; Cho, K.; Joannopoulos, J. *Phys. Rev. B: Condens. Matter Mater. Phys.* **1997**, *56*, 1354−1365.
(73) Martyna, G. J.; Klein, M. L.; Tuckerman, M. *J. Chem. Phys.* **1992**, *97*, 2635−2643.

DOI: 10.1021/jacs.7b01398
J. Am. Chem. Soc. 2017, 139, 7273−7286